



Development of magnetism in the solid solution of $\text{Ce}_{1-x}\text{Pr}_x\text{AlGe}$: From magnetic topology to spin glass

Pascal Puphal ^{1,*}, Sarah Krebber,¹ Emmanuelle Suard,² Robert Cubitt,² Chennan Wang,³ Tian Shang,¹ Victor Ukleev ⁴, Jonathan S. White,⁴ and Ekaterina Pomjakushina¹

¹Laboratory for Multiscale Materials Experiments, Paul Scherrer Institute, 5232 Villigen, Switzerland

²Institut Laue-Langevin BP 156, 38042 Grenoble Cedex 9, France

³Laboratory for Muon-Spin Spectroscopy, Paul Scherrer Institut, 5232 Villigen, Switzerland

⁴Laboratory for Neutron Scattering and Imaging, Paul Scherrer Institute, 5232 Villigen, Switzerland



(Received 18 February 2020; accepted 26 May 2020; published 8 June 2020)

We investigate the macroscopic and microscopic physical properties of the solid solution of $\text{Ce}_{1-x}\text{Pr}_x\text{AlGe}$. The series tunes from CeAlGe with its multi- \vec{k} structure and a major moment in the ab plane, to PrAlGe with an easy c -axis ferromagnetic ground state coexisting with a low density of nanoscale textured magnetic domain walls. Using AC, DC susceptibility, resistivity, specific heat, muon spin relaxation/rotation, and neutron scattering we analyze the magnetic ground state of the series. We provide further evidence supporting our previous claim for spin-glass-like properties in pure PrAlGe . With the introduction of Pr to CeAlGe the finite magnetic field required to stabilize the topological multi- \vec{k} magnetic phase for $x = 0$ becomes suppressed. The crossover between the two end-member ground states occurs in the vicinity of $x = 0.3$, a region where we further anticipate the field-induced topological magnetic phase for $x < 0.3$ to become the zero field ground state.

DOI: [10.1103/PhysRevB.101.214416](https://doi.org/10.1103/PhysRevB.101.214416)

I. INTRODUCTION

The polar magnet family RAIGe ($R = \text{Ce}, \text{Pr}$) [1] was predicted to offer remarkable tunability where type-I, type-II inversion-breaking, and time-reversal-breaking types of ferromagnetic Weyl semimetal states are all available. Weyl semimetals are a new class of topological conductors where in the bulk, conduction and valence bands cross at discrete singular points known as Weyl points [2].

While ternary LaPtSi -type ($I4_1md$) RAIGe alloys were already discovered in 1992 [3] the interest of these systems in the context of topological states has only been realized in 2018 [1]. Until recently only structural, specific heat, and magnetization data were published on CeAlGe polycrystalline samples [3–5] while for PrAlGe only the crystal structure had been studied previously [6]. Since the theoretical proposal of a Weyl state in these materials however, the interest in the two candidates has been recently ignited [7–10]. We were able to grow stoichiometric single crystals of both CeAlGe ($T_C = 5$ K) and PrAlGe ($T_C = 16$ K) [7] by floating zone growth and probing their magnetic structures using small-angle neutron scattering (SANS) and neutron powder diffraction (NPD). Other reported experimental studies were done on Al self-flux grown crystals which often present an Al enrichment and lead to different physics [7–9]. While PrAlGe presents the expected easy c -axis ferromagnetic ground state [11], for CeAlGe we discovered a surprisingly complex incommensurate (IC) multi- \vec{k} structure with a field induced topological magnetic state [12].

Here we present the magnetic ground state evolution tuned by chemical substitution in polycrystalline materials of the $\text{Ce}_{1-x}\text{Pr}_x\text{AlGe}$ solid solution. We performed a detailed magnetic characterization, analyzing AC, DC susceptibility, specific heat, transport, muon spin resonant relaxation/rotation (μSR) spectroscopy, as well as neutron scattering results. As our main result, we find a crossover in the nature of the magnetic ground state at $x \approx 0.3$, where moreover the magnetic field-stabilized topological phase for x slightly above 0.3 likely becomes the zero field ground state for a small region of x .

II. EXPERIMENTAL DETAILS

The polycrystalline samples were prepared by arc melting with a compact arc melter MAM-1, the three starting elements Ce/Pr, Al, and Ge of a minimum purity of 99.99% for homogeneity. X-ray fluorescence (XRF) spectra were recorded using the Orbis microXRF analyzer from EDAX. AC- and DC-magnetic susceptibility were carried out in a range of 1.8–400 K, 0–7 T, and 0.02–1480 Hz, using a Quantum Design Magnetic Property Measurements System (MPMS). Additionally AC- and DC-magnetic susceptibility measurements, resistivity, and specific heat measurements were carried out in the range of 1.8–300 K and 0–9 T, 10–10000 Hz on a Physical Property Measurement System (PPMS). Neutron diffraction experiments were done at beamlines at Institute Laue-Langevin (ILL): a D11 small-angle neutron scattering (SANS) beamline in the range of 1.6–20 K with a wavelength of $\lambda = 4.6$ Å using four polycrystalline ingots of $\text{Ce}_{1-x}\text{Pr}_x\text{AlGe}$ each of around 300 mg glued on an aluminum plate with GE varnish and one powdered sample taken from

*pascal.puphal@psi.ch

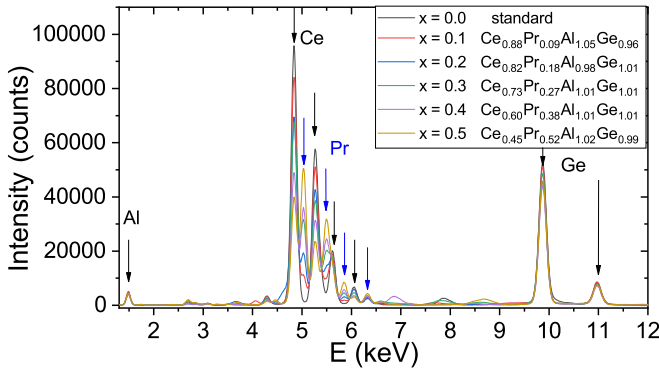


FIG. 1. XRF spectra of the polycrystalline series $\text{Ce}_{1-x}\text{Pr}_x\text{AlGe}$ measured on polished disks in vacuum normalized to the stoichiometric CeAlGe polycrystalline sample from Ref. [12].

D1B ($x = 0.2$) for comparison. D1B at $T = 1.6, 7,$ and 15 K with a wavelength of $\lambda = 2.525$ Å, as well as D2B $T = 300$ K using $\lambda = 1.59$ Å both on powdered polycrystalline samples of 2 g each loaded into indium sealed vanadium cans in a helium glovebox. Pressed pellets of powdered polycrystalline ingots of PrAlGe , CeAlGe , and $\text{Ce}_{0.7}\text{Pr}_{0.3}\text{AlGe}$ of 5 mm diameter were measured on the GPS instrument at the Swiss Swiss Muon Source ($S\mu S$) at PSI, in zero magnetic field (ZF) and temperatures down to 1.6 K.

III. ELEMENTAL ANALYSIS (EDS)

A detailed XRF study was performed to analyze carefully the compositions of all polycrystalline materials. This characterization is crucial, since both the structure-type and physical property transition temperatures can vary according to small compositional variations of $\text{RAI}_x\text{Ge}_{2-x}$ [5,8], which has a tremendous impact on the physical properties [7]. For the XRF study, we used a CeAlGe polycrystalline sample characterized in detail by XRF, energy dispersive spectroscopy (EDS), and neutron diffraction [12] as a standard.

In case of the polycrystalline materials the issues faced for self-flux growth do not exist and all samples are perfectly homogenous stoichiometric ingots as determined from the XRF data (see Fig. 1). The shown data are single point measurements with a 30 μm wide beam counted for 1 h in vacuum. No averaging was performed, as we saw no variation between the samples within uncertainty (checked by detailed mapping of a large polished area). The off-stoichiometry of the determined compositions and listed in the legend of Fig. 1 is maximally 0.05, and is below the 2 at % standard error of any elemental analysis. Furthermore, this XRF analysis was cross checked with an EDS analysis in a scanning electron microscope (SEM) which confirms perfect sample stoichiometries within uncertainty.

IV. CRYSTAL STRUCTURE

AlGe was first reported to crystallize in the α - ThSi_2 structure type with space group $I4_1/amd$ (No. 141) [3], with later studies instead proposing the LaPtSi structure type [5,6] with a body-centered polar tetragonal space group $I4_1md$ (No. 109). The structures are shown on the right part of Fig. 2. As

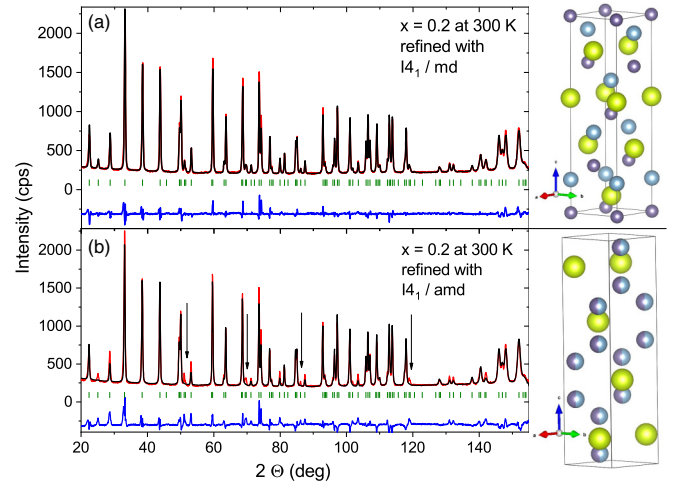


FIG. 2. Rietveld refinement of $\text{Ce}_{0.8}\text{Pr}_{0.2}\text{AlGe}$ NPD pattern measured at room temperature with a wavelength of 1.59 Å on D2B for two structures reported for CeAlGe : (a) $I4_1md$ and (b) $I4_1amd$, where arrows highlight the reflexes missing intensity. On the right part the corresponding crystal structure is shown, with Ce in green, Al in blue, and Ge in purple.

apparent from Rietveld refinements done using the Fullprof suite [13] displayed in Fig. 2 both structures result in different intensity distributions in neutron diffraction, where the main difference for the $I4_1/amd$ is highlighted by arrows. From these Rietveld refinements of neutron diffraction data, we find the $\text{Ce}_{1-x}\text{Pr}_x\text{AlGe}$ series forms a solid solution with a stable $I4_1md$ (No. 109) structure realized for all x . The structure is stable down to low temperatures, and a linear increase of the lattice constant with substitution following Vegard's law (see Table I). Thus we can confirm that for the whole series of $\text{Ce}_{1-x}\text{Pr}_x\text{AlGe}$ with a stoichiometric Al-Ge ratio the LaPtSi -type structure is realized, since powder neutron diffraction allows us to differentiate conclusively between the two candidate structure types.

V. MAGNETIC PROPERTIES

After having proven stoichiometric composition of the samples, we next turn to the detailed characterization of the magnetic properties of $\text{Ce}_{1-x}\text{Pr}_x\text{AlGe}$ in the temperature range from 1.6 to 400 K. As published recently [12], magnetic Ce ions in CeAlGe order incommensurately below 4.5 K with a unique multi- \vec{k} ground state, i.e., spin texture that is characterized by a periodic array of regions for which the magnetic topological winding number is either $+1/2$ or $-1/2$, and cancels when averaged over the entire sample. PrAlGe , on the other hand, orders predominantly ferromagnetically along the c -axis, and presents a small fraction of a coexisting nanoscale-sized domain walls involving moments tilted away from the c -axis best seen in SANS at low q values.

Figure 3 shows the phase diagram for the solid solution series constructed from data presented in this paper. We find a slow change between the end component ground states with a continuous shift of T_N resulting in an overlap at a substitution level of $x = 0.3$. With the introduction of Pr to CeAlGe we first find no strong influence on the ground state, but already

TABLE I. Rietveld refinement results of the three powder samples of $\text{Ce}_{1-x}\text{Pr}_x\text{AlGe}$ measured at room temperature with a wavelength of 1.59 \AA on D2B and at 15 K with a wavelength of 2.52 \AA on D1B.

T (K)	300			15		
	0.2	0.4	0.6	0.2	0.4	0.6
a (\AA)	4.27884(1)	4.27449(1)	4.26957(2)	4.26003(9)	4.26290(7)	4.25638(9)
c (\AA)	14.69229(9)	14.68619(8)	14.68354(10)	14.65517 (39)	14.66125(32)	14.64836(38)
z_R	0.59270(20)	0.59401(18)	0.59504(19)	0.59483(38)	0.59140(29)	0.59308(35)
z_{Al}	0.17626(17)	0.17795(16)	0.17896(17)	0.17432(36)	0.17127(27)	0.17738(32)
z_{Ge}	0.01001(17)	0.01131(16)	0.01240(18)	0.01319(36)	0.00642(28)	0.01246(33)
R factor	3.37	3.26	3.09	4.46	3.52	3.47

a linearly increasing size of the bulk moment (see Sec. VB). A second transition emerges from Pr spins due to glasslike behavior coexisting with the incommensurately ordered Ce moments, which is suppressed for $x \geq 0.3$ as seen in the T_N decrease. With further increase of the Pr content ($x \geq 0.4$) all moments, including those due to Ce, align ferromagnetically with the Pr ions presenting the nanoscale textured magnetic domain walls as reported in Ref. [11]. From then on the ferromagnetic ordering temperature and moment increase in a linear fashion with x . In addition to these ground states we found in SANS for the mixed system in $x = 0.3$ a suppression of the low q scattering below 3 K, indicating a fully aligned ground state, which is discussed in detail in Sec. VI. We find evidences of this additional low temperature transition in C/T drawn from the specific heat as a second maximum in all samples, which decreases in temperature with increasing x (see Sec. VC). The field dependence of the multi- \vec{k} ground state is sketched in the inset of Fig. 3, which predicts a

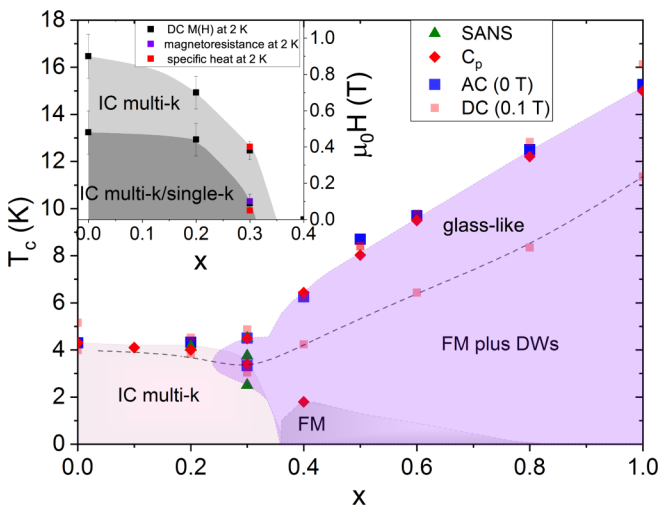


FIG. 3. Resulting phase diagram for $\text{Ce}_{1-x}\text{Pr}_x\text{AlGe}$ solid solution. The labeled magnetic phases are IC multi- \vec{k} : incommensurate magnetic multi- \vec{k} ground state determined for CeAlGe [12], FM plus DWs: a predominantly easy c -axis ferromagnet with low density of nanoscale domain walls, and FM: uniform ferromagnet. The points of the dashed line are extracted from the temperature derivative of the susceptibility [see Fig. 10(a)]. The inset shows the field dependence drawn from the derivatives of the $M(H)$ curves shown in Fig. 10(b).

possible stoichiometry, where the magnetic field-induced phase that generates a topological Hall effect signal [12] upon a field applied along the c -axis is stable without an external field. As here the data are drawn from polycrystalline material, the concerning critical fields remain to be verified for single crystals (for more details see Sec. VB).

A. AC susceptibility

The continuous tuning of the magnetic ground state with x is best seen in the AC-susceptibility data of the full series of the $\text{Ce}_{1-x}\text{Pr}_x\text{AlGe}$ solid solution shown in Fig. 4. Following the maximum of m' , we see the decrease of the multi- \vec{k} ground state, just when additionally the ferromagnetic ground state is realized at $x = 0.3$, while the increase of the latter one is apparent starting from $x > 0.3$. While only a subtle frequency dependence is seen in the maximum of m' , we observe a stronger shift of the left tail (visible in m'' described below). This likely reflects an external frequency-dependent response of the domain dynamics. The dependence is not apparent for $x = 0-0.2$, but starts in the vicinity of both ground states for the $x = 0.3$ sample. As previously reported also for PrAlGe [7] we find for the ferromagnetic ground state a really tiny shift in contrast to the results of Ref. [10].

The classification of the underlying ground states is obvious from a difference in the signal strength in $m''(T)$ and in a differing behavior in external field displayed in Fig. 5. The antiferromagnetically coupled incommensurate ground

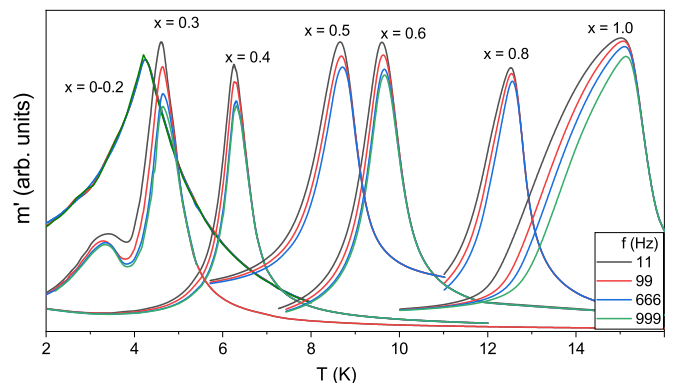


FIG. 4. AC-susceptibility data at 11, 99, 666, and 999 Hz for the full range of the substitution series measured in an AC field of 3.9 Oe in the low temperature range (2–16 K).

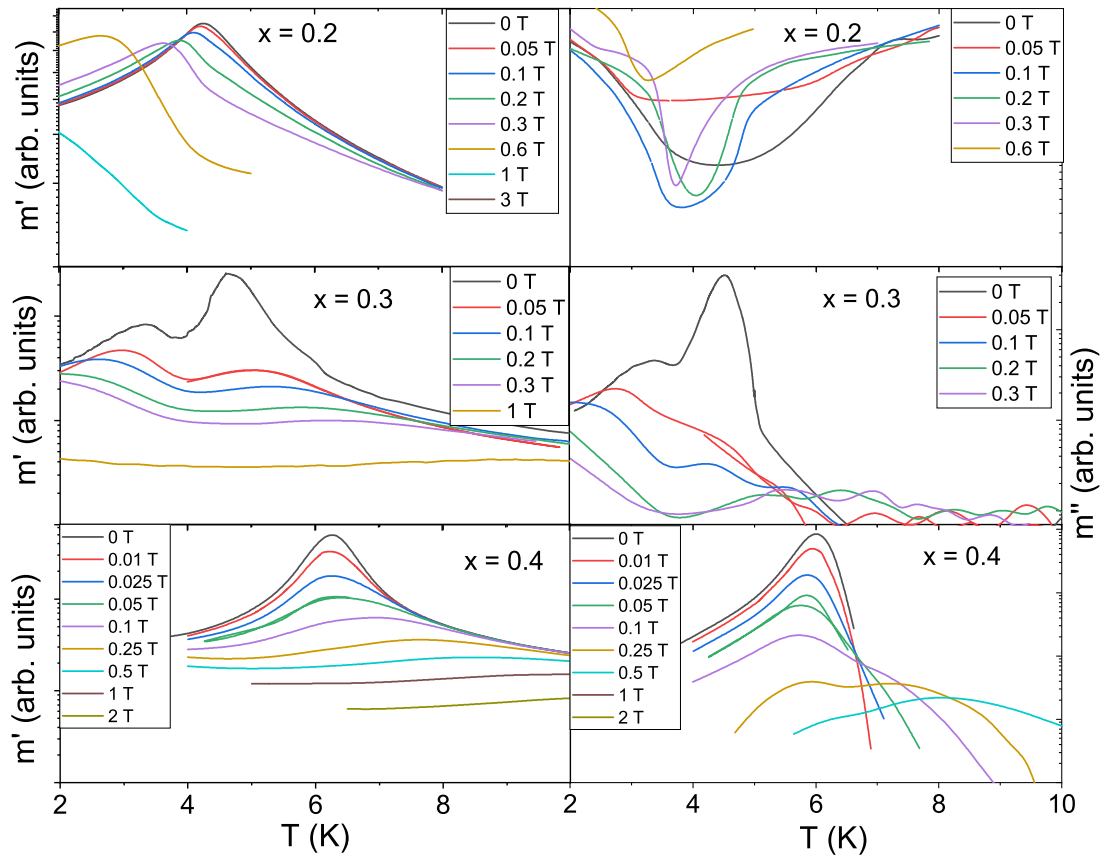


FIG. 5. Field dependence of the AC susceptibility versus temperature measured at a frequency of 997 Hz, with an AC field of amplitude of 3.8 Oe for three exemplary compositions $x = 0.2$ – 0.4 measured around the magnetic ordering transition.

state for $x < 0.4$ shifts down in temperature with increasing field, while the ferromagnetic ordering transition increases in temperature with increasing field. In addition, larger fields are necessary to suppress the susceptibility due to the incommensurately ordered phases compared to the ferromagnetic one as shown in Fig. 5.

For the magnetic ground state that is predominantly ferromagnetic with the low density of nanoscale domain walls, the AC susceptibility shows an aforementioned measurable frequency dependence, which is hardly visible in m' , shows up clearly as a shift of the maximum in the imaginary part m'' . We analyzed the response of m'' from the viewpoint of domain dynamics applying an Arrhenius law: $\tau = \tau_0 + \exp[E_b/(k_B T)]$ to fit the extracted relaxation times τ plotted versus the inverse maxima of m'' shown in Fig. 6(b). For spin glasses the increase of the relaxation times with decreasing temperature is faster than an Arrhenius law (upward curvature) [14]. This behavior can clearly be seen starting from a substitution amount of $x = 0.8$. The spin-glass system can better be described with the Vogel-Fulcher fit [15] following the equation $\tau = \tau_0 + \exp[E_b/k_B(T - T_{VF})]$, which is most apparent for the $x = 1.0$ case which does not follow the linear line [lowest plot in Fig. 6(b)]. Here we obtain a relaxation rate of $\tau_0 = 3.2(2) \times 10^{-9}$ s with an energy barrier of 15(3) K and a Vogel-Fulcher temperature of 12.86(8) K and $\tau_0 = 8(2) \times 10^{-15}$ s with an energy barrier of 31(2) K and a Vogel-Fulcher temperature of 11.00(4) K for $x = 0.8$. Both results are comparable to published ones of Pr containing metallic

spin glasses revealing $\tau_0 \sim 10^{-13}$ s and energy barrier of ~ 31 K [16].

B. DC susceptibility

With the clear image of the transition temperatures drawn from AC susceptibility we move to the peculiarities of the magnetism found in the substitution series analyzed by DC susceptibility. As both CeAlGe and PrAlGe have a ferromagnetic c coupling and an antiferromagnetic ab coupling of comparable size seen in the Curie-Weiss fits of data obtained on single crystals [7], for polycrystalline samples one finds a Curie-Weiss temperature close to 0. For CeAlGe with $\Theta_W^{\parallel c} = 10$ K and $\Theta_W^{\parallel a} = -42$ K [7] various results for polycrystalline materials are reported depending on the orientation and stoichiometry $\Theta_W = -13.5$, -25 , and -3.5 K [4,5,8]. For PrAlGe we found $\Theta_W^{\parallel c} = 36$ K and $\Theta_W^{\parallel a} = -30$ K compared with values reported elsewhere of $\Theta_W^{\parallel c} = 30$ K and $\Theta_W^{\parallel a} = -18$ K [10], possibly enhanced by Al-Ge ratio variations. For the polycrystalline samples of the solid solution series we find a reasonable evolution of the Curie-Weiss temperature as one would expect for the slow increase of ferromagnetic contributions along the c direction. From fits to the data seen in Fig. 7, we obtain $\Theta_W^{0.2} = -9.1$ K, $\Theta_W^{0.4} = -2.55$ K, $\Theta_W^{0.6} = 0.55$ K, and $\Theta_W^{0.8} = 4.70$ K. With theoretical values for the moment size of Ce of $2.54 \mu_B$ going to $3.58 \mu_B$ the effective magnetic moments extracted from fitting high

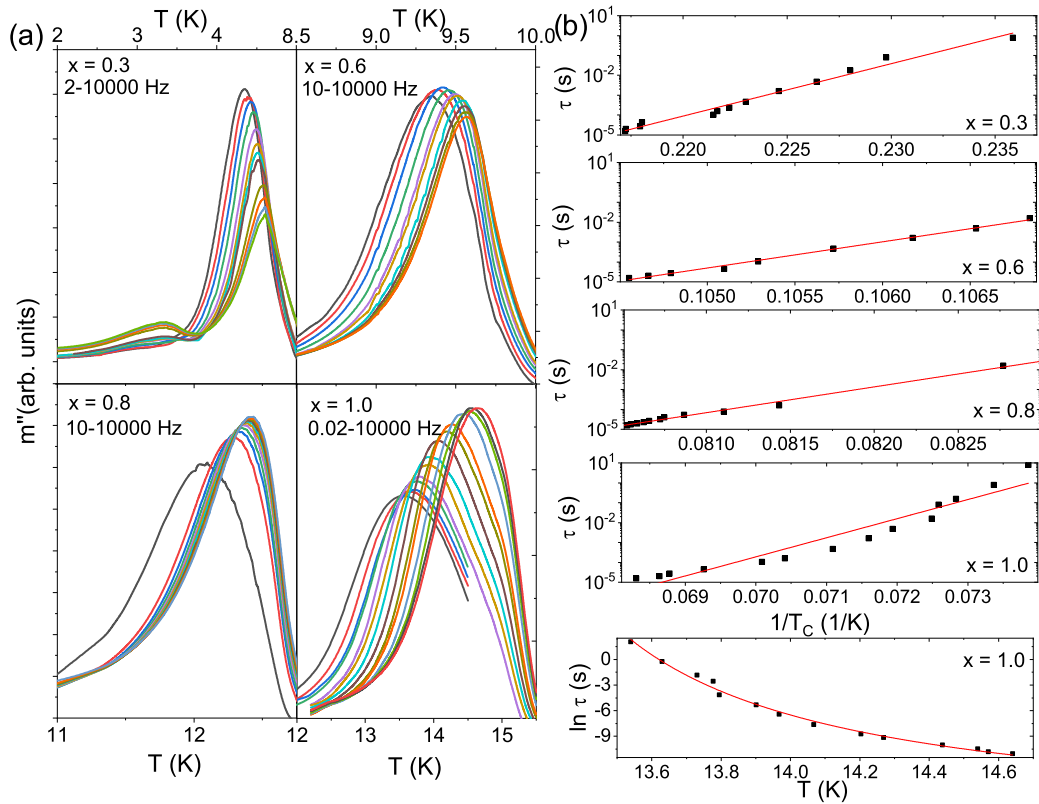


FIG. 6. (a) Imaginary part of the AC susceptibility measured on the polycrystalline compounds of $Ce_{1-x}Pr_xAlGe$ at various frequencies. (b) Relaxation time $\tau = 1/(2\pi f)$ plotted versus the inverse temperature of the extracted maxima in a semilogarithmic scale from AC-susceptibility measurements of $x = 0.3, 0.6, 0.8,$ and 1.0 . Red squares are from MPMS (QD) measurements, and black squares from a PPMS (QD). The lines are fits to the Arrhenius law given in the text.

temperature portion of the DC-magnetic susceptibility should vary from 2.78, 3.00, 3.20 to 3.40 μ_B for $x = 0.2, 0.4, 0.6,$ and $0.8,$ respectively. Indeed, the effective moment obtained from the Curie-Weiss fits yield: $\mu_{eff}^{0.2} = 2.73 \mu_B, \mu_{eff}^{0.4} = 2.99 \mu_B, \mu_{eff}^{0.6} = 3.09 \mu_B,$ and $\mu_{eff}^{0.8} = 3.3 \mu_B$. As seen in Fig. 8, the low temperature DC susceptibility shows the expected trend of increasing magnetization and ordering temperature while adding more Pr. Again the behavior can be divided into two kinds: while $x < 0.4$ shows a downturn in field cooling (FC), we find, as expected for a ferromagnetic ground state, a satura-

tion to a finite magnetization starting from $x \geq 0.4$. For all $x,$ the zero field-cooled (ZFC) measurement shows an increase of the magnetization with temperature up to the ordering temperature. While pure CeAlGe and low x concentrations and the low substitution of Pr presents a tiny hysteresis at

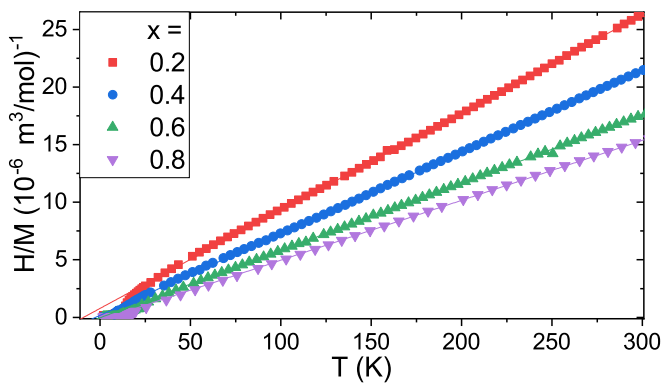


FIG. 7. Inverse magnetization versus temperature in the high temperature range measured at low fields of 0.1 T with applied Curie-Weiss fits.

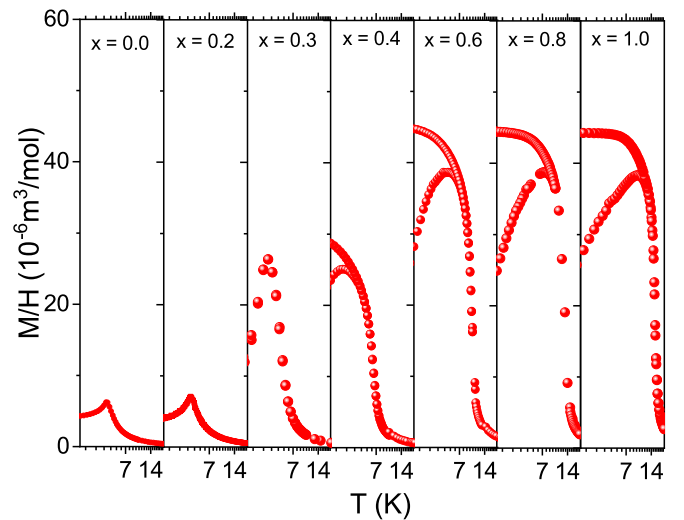


FIG. 8. Magnetization versus temperature in the low temperature range (2–20 K) measured at low fields of 0.1 T both in field-cooled (upper curve) and zero field-cooled (lower curve) manner.

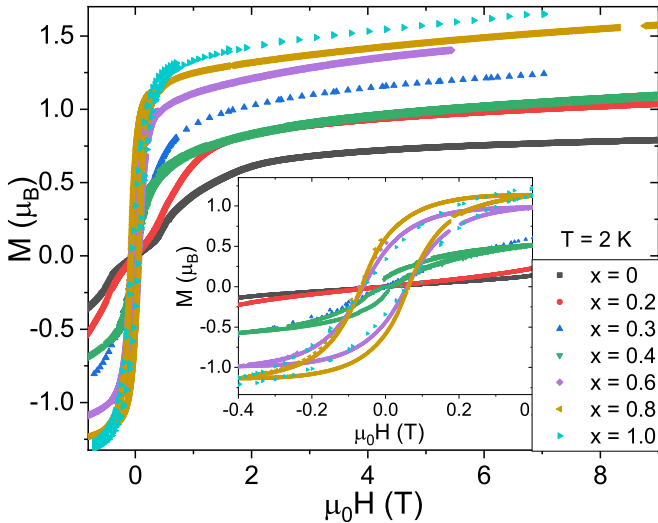


FIG. 9. Field dependence of the magnetization in the range -0.5 to 2 T of the magnetization measured on exemplary polycrystalline samples of the $\text{Ce}_{1-x}\text{Pr}_x\text{AlGe}$ series.

2 K [7], for the polycrystalline $x = 0.3$ sample we find no gap between FC and ZFC measurements, despite the significant frequency dependence of the AC susceptibility indicating domain dynamics as shown in the previous subsection.

Before analyzing the transitions in more detail we look into the hysteretic behavior seen in field-dependent DC susceptibility. In Fig. 9 the magnetization measured at 2 K for field sweeps is shown in between -0.7 and 7 T. We find as expected an increase in the saturation magnetization at high fields that scales with the Pr amount, however the monotonic behavior is discontinuous at $x = 0.4$ possibly due to the only substitution amount being in range of the fully FM order shown in the phase diagram. In the $M(H)$ curve the underlying ground state is easily extracted by the fact that once the ferromagnetic order with domain walls is realized a hysteresis is observed. In agreement with the AC data we find a sudden change in the magnetization behavior with a substitution amount from $x = 0.4$, as starting from $x \geq 0.4$ the hysteresis emerges with a similar coercive field for $x \geq 0.6$ of roughly 0.064 T.

Derivatives of the DC-susceptibility data as shown in Fig. 10 enables both a visualization and determination of the critical transitions for the temperature, as well as the fields which are added to the phase diagram in Fig. 3. In the temperature derivative we always find a positive and a negative maximum, which for $x = 1$ can be accounted to a spin-glass-like transition and a subsequent spin reorientation as shown in Ref. [7]. This reorientation transition is only visible in small fields (here 50 Oe) and can be tracked for all substitution amounts even in pure CeAlGe. These data amount to the dashed line in the phase diagram (see Fig. 3). For single crystals of CeAlGe two different metamagnetic transitions are observed in each field direction, where only the two with field along the c -axis surround a topological magnetic phase [7, 12]. As here we measure the polycrystalline materials two critical fields for each orientation lead to kinks. For the $x = 0$ polycrystalline case we can compare the two clear kinks of the low field metamagnetic transitions at 0.35 and 0.55 T seen in

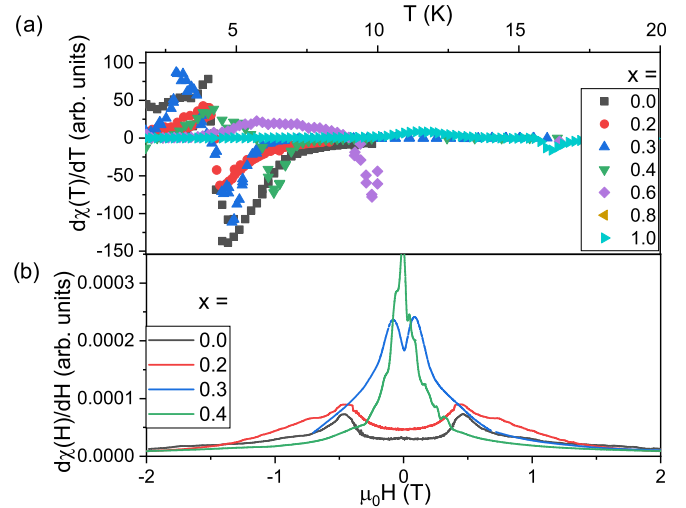


FIG. 10. (a) Temperature derivative and (b) field derivative of the DC susceptibility, revealing x dependence of the transition temperatures and fields.

Fig. 8 with the literature results obtained on single crystals (0.2 and 0.4 T, respectively) [7, 12]. Here we observe larger values as they are not corrected for demagnetization. From the derivatives one can clearly extract the low field transition region (both a and c direction) together as a maximum seen in Fig. 10(b). A second, smaller maximum is observed which matches values of the high field transition of the c direction. Although the exact values of the critical field are not apparent from the polycrystalline data, the general trend of the critical field can be studied with the substitution amount of Pr. We clearly observe a decrease of the low field metamagnetic transition and thus expect a zero field topological magnetic state for single crystals of a substitution amount slightly larger than $x = 0.3$.

C. Specific heat

From specific heat studies of the polycrystalline series we can identify two transitions. The spin reorientation seen in the derivative of the DC susceptibility is not observed in specific heat, as was already reported for PrAlGe [10]. However an additional signal at low temperatures is found from the vanishing of the nanoscale domain wall texture that we describe in the next section. The entropy released at the transition is for all cases around $S \approx R \ln 2$, when extrapolating the low temperature part of the specific heat for low x concentrations. However the entropy distribution varies with x as for PrAlGe the transition is less sharp. Due to crystal field splitting we expect an effective $S = 1/2$ state for CeAlGe. Thus the entropy in our transition of $S \approx R \ln 2$ describes a full order. The reduced size of the moment is due to a mixed valence of roughly 50% Ce^{4+} , which is nonmagnetic (see the Supplemental Information of Ref. [12]). For the spin-glass system PrAlGe an effective $S = 1$ is expected with an entropy of $S \approx R \ln(2S + 1)$. Of this entropy we observe only 63%, however part of the missing entropy might lie in the second maximum at lowest temperatures, which is already apparent by the upturn at lowest temperatures shown in the right panel

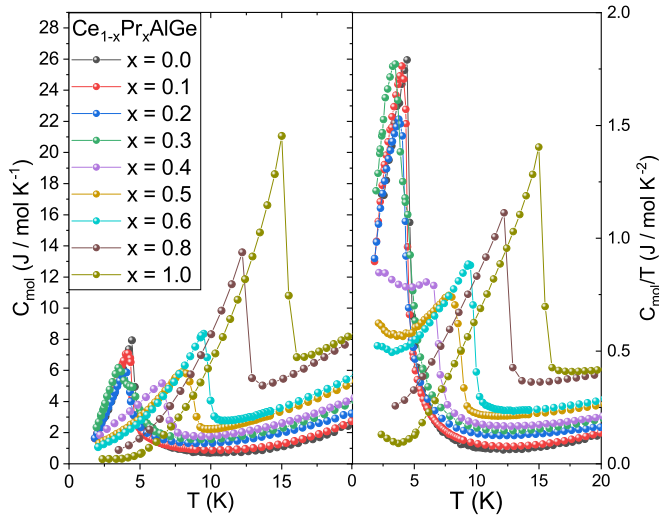


FIG. 11. Specific heat of the solid solution series $\text{Ce}_{1-x}\text{Pr}_x\text{AlGe}$ for the low Pr substituent in the range of 1.8–20 K in zero field. The right panel shows the same selected samples of the specific heat divided by temperature.

of Fig. 11. The temperature of the second maximum of $x = 0.3$ exactly matches the temperature of the disappearance of low q scattering seen in SANS (see Sec. VI) and indicates a possible spin reorientation to a fully aligned case without domain walls, shown as a gray area in the phase diagram (see Fig. 3).

VI. NEUTRON DIFFRACTION

In Fig. 12 we show the magnetic contribution, i.e., the difference pattern of the neutron powder diffraction data mea-

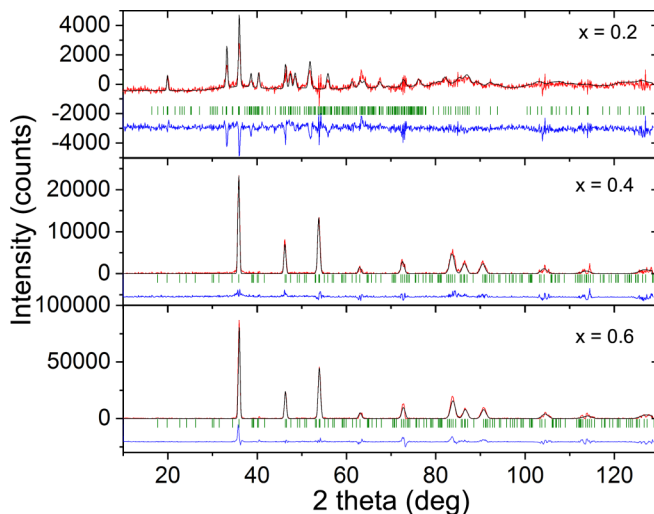


FIG. 12. NPD difference profiles obtained at DIB from $\text{Ce}_{0.8}\text{Pr}_{0.2}\text{AlGe}$, $\text{Ce}_{0.6}\text{Pr}_{0.4}\text{AlGe}$, and $\text{Ce}_{0.4}\text{Pr}_{0.6}\text{AlGe}$ at base $T = 1.6$ K below T_C , and at 15 K above T_C . The refinement of the magnetic profile is given in black. The blue line shows the difference between the refined model profile and the data. The row of green ticks denote possible positions for magnetic peaks according to the magnetic structure model.

sured below (1.6 K) and above (15 K) T_C with a wavelength of $\lambda = 2.525$ Å, of three compositions of $x = 0.2, 0.4, 0.6$. Similarly as for results obtained from bulk measurements, we find a sharp change of the ground state above $x > 0.3$, where the Ce moments presumably become aligned with the ferromagnetically ordered Pr ones. In contrast, for a low Pr substitution amount the incommensurate order of pure CeAlGe prevails. To determine the IC magnetic structure in $\text{Ce}_{0.2}\text{Pr}_{0.8}\text{AlGe}$ we used the Fullprof suite [13] to perform a detailed Rietveld refinement of the neutron powder diffraction (NPD) difference pattern against several symmetry-allowed models. The symmetry analysis shows that the magnetic structure model of highest symmetry is based on the full propagation star of \vec{k} which consists of four arms $\vec{k}_1 = \pm(a, 0, 0)$ and $\vec{k}_1 = \pm(0, a, 0)$. This corresponds to a multi- \vec{k} model described by the maximal symmetry superspace group $I4_1md1'$ ($a00$)000s(0a0)0s0s [12], and has just four refinable magnetic mode amplitude parameters. Via LeBail fitting we find for $x = 0.2$ a slightly larger \vec{k} vector of $a = 0.0785(1)$ compared to $a = 0.071(1)$ in the case $x = 0$. For $x > 0.3$ we find magnetic scattering only at scattering angles commensurate with the tetragonal point symmetry of the RAIge lattice, which can be described by a propagation vector $Q = 0$. As for PrAlGe [11] for the three symmetry-allowed magnetic structure models for $Q = 0$, we find the standard irreducible representation Γ_1 , that describes a ferromagnetic (FM) order with moments aligned with the c -axis, to solve our magnetic pattern for both $x = 0.4$ and $x = 0.6$. The size of the ferromagnetic moment refined from the data increases as expected with the larger Pr content $1.17(1) \mu_B$ ($x = 0.4$) and $1.77(1) \mu_B$ ($x = 0.6$) compared to $2.29(3) \mu_B$ for $x = 1$ [11].

To track the change of the microscopic magnetism with x in more detail we performed SANS measurements on polycrystalline ingots of the $\text{Ce}_{1-x}\text{Pr}_x\text{AlGe}$ series. The SANS images of reciprocal space clearly reveal a sharp change in the general form of low q magnetic scattering above $x > 0.3$. For $x < 0.3$, scattering is observed at finite wave vector in analogy with that seen for pure CeAlGe [12], and in the present polycrystalline samples displays either a ring- or Bragg-spotlike distribution. This scattering at finite wave vector disappears for $x > 0.3$, and instead we observe significant magnetic SANS to emerge at lowest q for $T < T_C$ similar as for PrAlGe following the phase diagram depicted in Fig. 3. This observation suggests that in addition to dominant easy c -axis ferromagnetic correlations, a coexisting nanoscale magnetic texture also exists in the samples of $\text{Ce}_{1-x}\text{Pr}_x\text{AlGe}$ for $x \geq 0.3$ analogously as for $x = 1$ and discussed in detail in Ref. [11]. In this case the intensity is distributed uniformly in azimuth around the origin, and falls monotonically over an extended range of $|q|$.

In addition, we find a low q scattering from the slightly misaligned domains already for $x = 0.2$ and 0.3 meaning that with the introduction of Pr to the structure, the ferromagnetic coupling part creates a separation in domains [see Fig. 13(b)]. From a proper normalization of the scattered intensity, we can generally track the increase of scattering contribution due to moment increase from Pr introduction, though we note that may be compensated by the different intensity distributions observed for $x = 0, 0.2$ (ringlike) that differ markedly from the almost Bragg-spotlike distribution observed from the $x =$

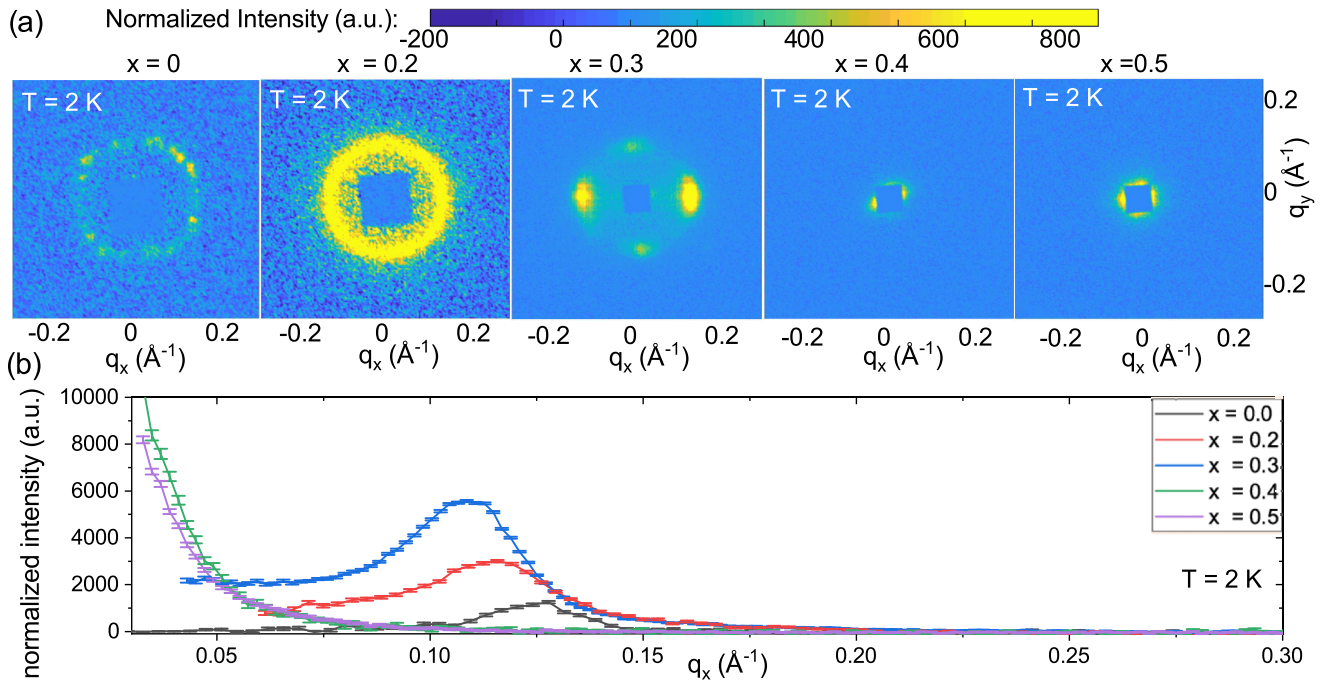


FIG. 13. (a) SANS magnetic scattering patterns for four polycrystalline ingots and one powder ($x = 0.2$) sample, where the intensity scaling is fixed on the same range for comparison. (b) Integrated intensities of the SANS patterns plotted versus the wave vector q normalized to the sample size so that intensities can be compared.

0.3 sample. By plotting the same integrated intensity versus temperature shown in Fig. 14, we find that the low q scattering vanishes below a certain temperature meaning that the Ce moments finally align with the Pr ones.

VII. MUON SPIN RELAXATION/ROTATION SPECTROSCOPY

To further explore the low-temperature magnetic properties of the $\text{Ce}_{1-x}\text{Pr}_x\text{AlGe}$ series, we conducted a zero field (ZF) μSR experiment down to 1.6 K. Almost 100% spin polarized

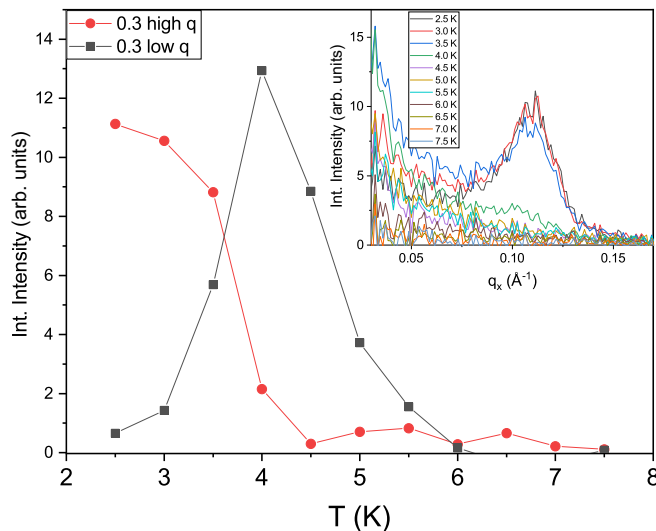


FIG. 14. Integrated intensities of the SANS patterns of $x = 0.3$ plotted versus temperature. In the inset the q dependent integrated intensities at various temperatures are shown.

surface muons carrying positive charges are implanted into the sample where they preferentially stop at the most electronegative location near Ge at time zero. The implanted muons relax via coupling with the local magnetic field at the muon site. The temporal evolution of the muon spin polarization is thereafter measured by the asymmetry of the decayed positrons which are emitted preferentially along the muon spin direction [17]. Figure 15 shows the muon time spectra of the $\text{Ce}_{1-x}\text{Pr}_x\text{AlGe}$ sample measured below and above the magnetic transition temperatures. For the $x = 1.0$ compound, the early time muon polarization shows a nonoscillatory and rapid decaying behavior. Meanwhile, the spectrum in the longer period of measurement remains nonrelaxing and stays around 1/3 of the total polarization. The spectra can be well ascribed with a two-component model for the static magnetic moments with a random distribution, i.e.,

$$P = \frac{1}{3} + \frac{2}{3} \exp[-(\lambda t)^\beta]. \quad (1)$$

The transverse 2/3 component is well fitted with a stretched exponential with $\beta \sim 0.5$. The obtained very large relaxation rate about $100 \mu\text{s}^{-1}$ evidences a highly incoherent magnetic structure, supporting the scenario of a freezing of the internal fields as evident in a spin-glass (SG)-like transition [7,11].

In case of CeAlGe ($x = 0$) [see Fig. 15(c)], the asymmetry plot shows a clear damped signal oscillating around 1/3 of the initial spin polarization. The data suggest the muon ensemble detects a coherent internal field induced by the ordered magnetic structure, which is present in the entire volume of the sample. Incommensurate magnetic orders such as spin density waves are best fit by a zeroth order Bessel function J_0 [18]. On the other hand, the polarization in the present case of a multi- \vec{k} incommensurate magnetic structure can be described equally

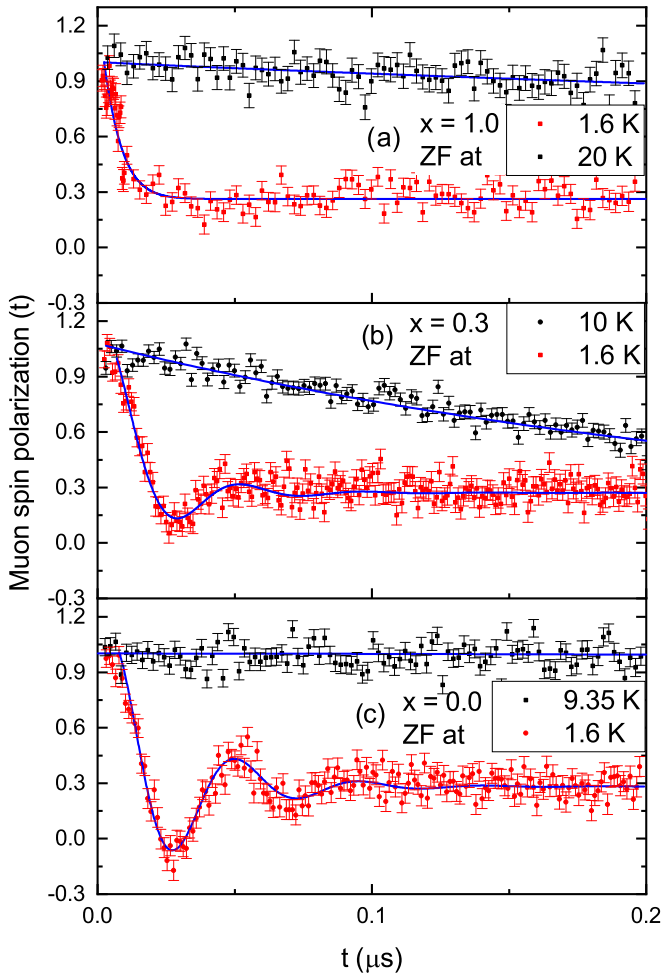


FIG. 15. Temperature evolution of the muon spin polarization in the (a) $x = 1$, (b) $x = 0.3$, and (c) $x = 0$ compound in zero field, at base temperature 1.6 K and far above the transition, i.e., 9.35, 10, and 25.2 K. The solid lines are fits according to Eqs. (1) and (2).

well by an exponentially decaying cosine:

$$P = \frac{1}{3} + \frac{2}{3} \exp(-\lambda t) \cos(\omega t). \quad (2)$$

The maximum frequency is centered at 22.3(3) MHz, while the one for PrAlGe is centered at 0 typical for a SG system. For the crossover stoichiometry of $\text{Ce}_{0.7}\text{Pr}_{0.3}\text{AlGe}$ [see Fig. 15(b)] we still observe oscillations, which are more strongly damped than for CeAlGe due to the additional PrAlGe character. The maximum frequency is 22(1) MHz and hence nearly unchanged compared to the $x = 0$ case. This suggests that incommensurate multi- k structures observed for $x = 0$ and $x = 0.3$ can be considered to be broadly similar, which is in agreement with data obtained from neutron scattering. From the muon data, we find generally large values of the relaxation rate for RAlGe. Due to the fast relaxation from the glassiness induced by Pr we find an increasing relaxation rate λ with increasing amount of Pr, which is a hallmark of the broadening of the distribution of the local magnetic fields. In the ordered phase at 1.6 K we find λ values of the fast decaying part for increasing x of: 37(1), 61(3), and finally 160(20) μs^{-1} for $x = 0.0, 0.3$, and 1.0.

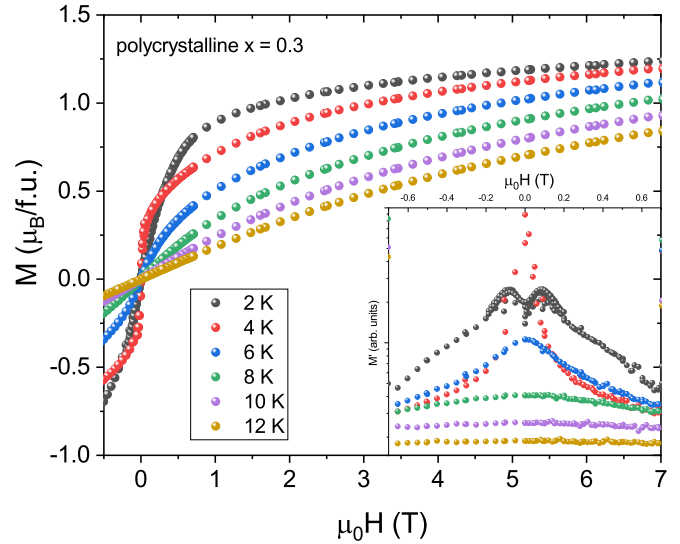


FIG. 16. Field dependence of the magnetization at various temperatures in the range of 0–7 T measured on a 28.4 mg ingot of the polycrystalline $\text{Ce}_{0.7}\text{Pr}_{0.3}\text{AlGe}$ sample.

VIII. CROSSOVER REGION AROUND $x = 0.3$

Around $\text{Ce}_{0.7}\text{Pr}_{0.3}\text{AlGe}$ we find the most complex part in the phase diagram, as we find an overlap of low q scattering arising from ferromagnetic domains and the multi- \vec{k} scattering around 0.11 \AA between 3 and 4 K as well as separated parts of each as shown in Fig. 14. Indicating separate regions of the two ground states. We focus now on the details of this compositional area by analyzing the field dependent magnetization and resistivity. As one might deduce from the indication of frequency-dependent domain dynamics by AC susceptibility at 4 K, where we are in the low q scattering maximum seen in Fig. 14, we find a tiny hysteresis for $x = 0.3$ seen in the red curve of Fig. 16. This hysteretic behavior however vanishes when the sample is cooled down to 2 K, and for which the low q scattering disappears and we only realize the multi- \vec{k} ground

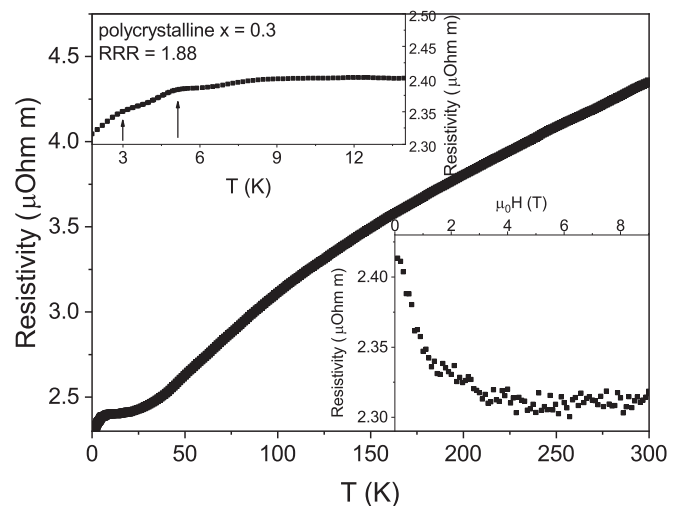


FIG. 17. Temperature dependence of the resistivity on a polycrystalline ingot polished to a flat needle. The inset shows the field dependent resistivity measured at 2 K.

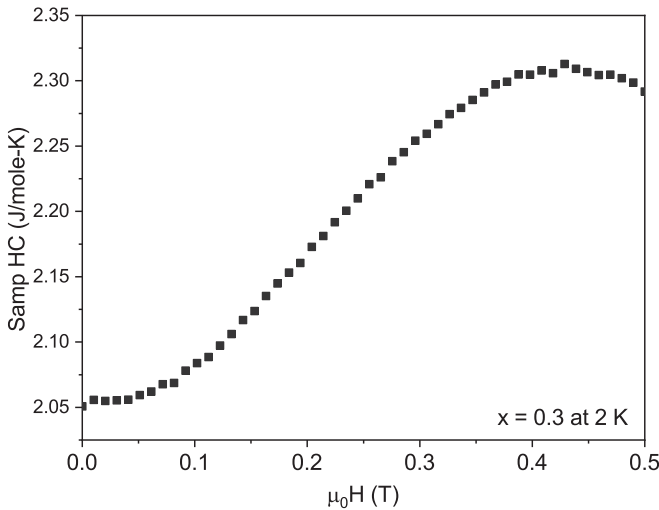


FIG. 18. Specific heat of the $x = 0.3$ sample measured at 2 K with increasing fields up to 0.5 T.

state. Only at this temperature the metamagnetic transition becomes apparent, visible in the inset of Fig. 16.

For the $RAI\text{Ge}$ samples a relatively low residual resistivity ratio (RRR) of 1–2 is reported, considering it is a semimetal [7,8,10]. So, unsurprisingly we find a decrease of the resistivity with decreasing temperature of the polycrystalline $Ce_{0.7}Pr_{0.3}Al\text{Ge}$ sample with a RRR value of 1.88 shown in Fig. 17. Similar to the end compounds we see the magnetic transition displayed on the inset, which in this case even indicates a double peak with maxima both at 2.8 and 5 K in good agreement with anomalies observed in AC susceptibility and SANS measurements (see Fig. 14). Similar to $CeAl\text{Ge}$ we find a negative magnetoresistance, the metamagnetic transition is seen in two kinks highlighted by arrows at 0.1 and 0.4 T. In pure $CeAl\text{Ge}$, these two metamagnetic transitions occur at higher fields of 0.5 and 0.8 T, respectively (see Fig. 3 inset), and over this range of magnetic field a topological magnetic phase that generates a topological Hall signal is stabilized [12]. The present study shows that the two metamagnetic transition fields become suppressed with increasing x . In a field scan of the specific heat shown in Fig. 18 we observe a signal increase exactly at the critical fields extracted from our $M(H)$ curves. Supporting our deduction of possible reduced critical fields.

We thus anticipate that for a further small increase of x beyond 0.3, the field-induced topological phase for $x = 0$ can be stabilized as a zero field ground state.

IX. SUMMARY

The solid solution $Ce_{1-x}Pr_xAl\text{Ge}$ preserves the two ground states of the parent compounds up to the overlapping region around $Ce_{0.7}Pr_{0.3}Al\text{Ge}$, which represents the general crossover composition between the end member ground states. While for $x < 0.3$ the multi- \vec{k} ground state of $CeAl\text{Ge}$ remains nearly unchanged in its magnetic ordering temperature the metamagnetic transition fields shift, leading to the possibility to stabilize the field-induced topological phase as a zero field ground state when x is just above 0.3. The predominantly ferromagnetic ground state of $PrAl\text{Ge}$ decreases in T_C with increasing amount of Ce, so does the moment size, while the energy barrier of the domain formation increases, which enables a fully FM aligned Γ -point solution at lowest temperatures for the mixed system. With $Ce_{0.7}Pr_{0.3}Al\text{Ge}$ we find an interesting compound where in a limited temperature range the interplay between these ground states can be studied. It provides a candidate Weyl semimetal that enables a tuning of the bands via a ferromagnetic ground state from 4 to 5 K and multi- \vec{k} order below 3 K.

ACKNOWLEDGMENTS

The authors thank Hubertus Luetkens, Stephan Al-lenspach, and Vladimir Pomjakushin for fruitful discussions. This work is partly based on experiments performed at the Institut Laue-Langevin (ILL), Grenoble, France. Neutron data collection [19] using D11 and D1B at ILL took place with support from proposal 5-31-2660. This work is based on experiments performed at the Swiss Muon Source $S\mu\text{S}$, Paul Scherrer Institute, Villigen, Switzerland. Part of the magnetic measurements were carried out on the PPMS/MPMS devices of the Laboratory for Multiscale Materials Experiments, Paul Scherrer Institute, Villigen, Switzerland, as well as the PPMS device of the Kristall- und Materiallabor, Goethe University Frankfurt am Main, Germany. V.U. and J.S.W. acknowledge financial support from the SNSF Sinergia network NanoSkyrmionics (Grant No. CRSII5_171003), SNSF Projects No. 200021_188706 and No. 200021_188707.

-
- [1] G. Chang, B. Singh, S.-Y. Xu, G. Bian, S.-M. Huang, C.-H. Hsu, I. Belopolski, N. Alidoust, D. S. Sanchez, H. Zheng, H. Lu, X. Zhang, Y. Bian, T.-R. Chang, H.-T. Jeng, A. Bansil, H. Hsu, S. Jia, T. Neupert, H. Lin, and M. Z. Hasan, *Phys. Rev. B* **97**, 041104(R) (2018).
 - [2] H. Weyl, *Z. Phys.* **56**, 330 (1929).
 - [3] S. Dhar, S. Pattalwar, and R. Vijayaraghavan, *J. Magn. Magn. Mater.* **104–107**, 1303 (1992).
 - [4] H. Flandorfer, D. Kaczorowski, J. Gröbner, P. Rogl, R. Wouters, C. Godart, and A. Kostikas, *J. Solid State Chem.* **137**, 191 (1998).
 - [5] S. Dhar and S. Pattalwar, *J. Magn. Magn. Mater.* **152**, 22 (1996).
 - [6] E. Gladyshevskii, N. Nakonechna, K. Cenzual, R. Gladyshevskii, and J.-L. Jorda, *J. Alloys Compd.* **296**, 265 (2000).
 - [7] P. Puphal, C. Mielke, N. Kumar, Y. Soh, T. Shang, M. Medarde, J. S. White, and E. Pomjakushina, *Phys. Rev. Mater.* **3**, 024204 (2019).
 - [8] H. Hodovanets, C. J. Eckberg, P. Y. Zavalij, H. Kim, W.-C. Lin, M. Zic, D. J. Campbell, J. S. Higgins, and J. Paglione, *Phys. Rev. B* **98**, 245132 (2018).

- [9] T. Suzuki, L. Savary, J.-P. Liu, J. W. Lynn, L. Balents, and J. G. Checkelsky, *Science* **365**, 377 (2019).
- [10] B. Meng, H. Wu, Y. Qiu, C. Wang, Y. Liu, Z. Xia, S. Yuan, H. Chang, and Z. Tian, *APL Mater.* **7**, 051110 (2019).
- [11] D. Destraz, L. Das, S. S. Tsirkin, Y. Xu, T. Neupert, J. Chang, A. Schilling, A. G. Grushin, J. Kohlbrecher, L. Keller, P. Puphal, E. Pomjakushina, and J. S. White, *npj Quantum Mater.* **5**, 5 (2020).
- [12] P. Puphal, V. Pomjakushin, N. Kanazawa, V. Ukleev, D. J. Gawryluk, J. Ma, M. Naamneh, N. C. Plumb, L. Keller, R. Cubitt, E. Pomjakushina, and J. S. White, *Phys. Rev. Lett.* **124**, 017202 (2020).
- [13] J. Rodríguez-Carvajal, *Physica B: Condens. Matter* **192**, 55 (1993).
- [14] E. Vincent and V. Dupuis, *Frustrated Materials and Ferroic Glasses* (Springer International, Berlin, 2018), pp. 31–56.
- [15] G. S. Fulcher, *J. Am. Ceram. Soc.* **8**, 339 (1925).
- [16] Y. T. Wang, H. Y. Bai, M. X. Pan, D. Q. Zhao, and W. H. Wang, *Phys. Rev. B* **74**, 064422 (2006).
- [17] S. J. Blundell, *Contemp. Phys.* **40**, 175 (1999).
- [18] J. Sugiyama, Y. Ikedo, K. Mukai, J. H. Brewer, E. J. Ansaldo, G. D. Morris, K. H. Chow, H. Yoshida, and Z. Hiroi, *Phys. Rev. B* **73**, 224437 (2006).
- [19] <https://doi.org/10.5291/ILL-DATA.5-31-2660>.